CCFE
CULHAM CENTRE FOR FUSION ENERGY

UK Atomic Energy Authority

UKAEA-CCFE-PR(24)204

Jie Hou, Duc Nguyen-Manh, Jun Song

Deuterium trapping and desorption by vacancy clusters in irradiated Mo from object kinetic Monte Carlo simulations

Deuterium trapping and desorption by vacancy clusters in irradiated Mo from object kinetic Monte Carlo simulations

Jie Hou, Duc Nguyen-Manh, Jun Song

This is a preprint of a paper submitted for publication in
Journal of Nuclear Materials

Deuterium trapping and desorption by vacancy clusters in irradiated Mo from object kinetic Monte Carlo simulations

Jie Hou[1,2], Duc Nguyen-Manh[3*], Jun Song[2*]

1 College of Materials Science and Engineering, Hunan University, Changsha, 410082, China

2 Department of Mining and Materials Engineering, McGill University, Montreal, Quebec, H3A 0C5, Canada

3. Materials Division, United Kingdom Atomic Energy Authority, Abingdon, OX14 3DB, United Kingdom

Abstract

We present a computational study employing Object Kinetic Monte Carlo simulations to investigate the behavior of D in self-irradiated Mo samples. Our simulations reveal that vacancy clusters contributing significantly to D diffusion, trapping, and desorption behavior. It is found that vacancy clusters play an important role in slowing the diffusion of D within the irradiated materials, which can be represented by an effective trapping energy that associated with mobile D atom interacting with the multiple types of vacancy clusters. Furthermore, we analyze the thermal desorption spectrum of D from irradiated Mo samples, demonstrating a saturation effect in D retention at higher damage levels. Notably, the presence of vacancy clusters significantly influences the thermal desorption spectrum and leads to the observation of negative desorption rates at specific temperatures. We also investigate the D desorption behavior under constant temperature storage conditions, revealing a non-exponential desorption rate with a 1/t decrease over time. Our study sheds light on the complex interplay between D and vacancies/vacancy clusters in irradiated materials, highlighting the importance of considering vacancy clusters in modeling D retention and desorption processes.

1. Introduction

The interaction between fusion plasma and materials stands as a paramount concern in the advancement of nuclear fusion technology [1, 2]. In future magnetic confinement fusion reactors, plasma facing materials (PFM) will endure intense fluxes of deuterium-tritium (D-T) plasma, prompting the retention of fuel within the PFM, which is a critical for stable operation of the reactor [3-5]. molybdenum

(Mo) is among the promising candidates for PFM, presently employed as a first-wall material in Experimental Advanced Superconducting Tokamak (EAST), and earmarked for utilization in plasma diagnostic systems within International Thermonuclear Experimental Reactor (ITER). Despite the inherently low hydrogen (H) isotope solubility in pristine Mo [6], it is well-established that irradiation damages significantly augment the retention rate of hydrogen isotopes in materials [3, 7]. This enhanced retention rate raises concerns regarding fuel retention in Mo when subjected to the high-energy neutron bombardment inherent in fusion reactions.

In contrast to other PFM candidates such as tungsten (W), the investigation into H retention in irradiated Mo has received comparatively less attention. Early experiments predominantly focused on studying the behavior of hydrogen isotopes in unirradiated Mo samples[8, 9] or Mo sample irradiated with low energy ion [9-11]. A recent study by Lavrentiev et al. delved into the behavior of D retention in Mo irradiated by 1 MeV self-ions, reaching a damage level of 1 displacement per atom (dpa) [7]. This investigation revealed a prominent peak in the thermal desorption spectrum (TDS) at approximately 550 K. While these experimental endeavors have provided valuable insights into H retention and desorption in Mo, accurate interpretation of these experimental data necessitates a precise understanding of the interaction between H and irradiation-induced defects, particularly vacancy-type defects known to exert a strong trapping effect on H isotopes. This motivated density functional theory (DFT) investigations concerning the interaction between H and monovacancies [12-15]. Numerous theoretical studies have consequently utilized the monovacancy trapping mechanism to model H retention and desorption phenomena [7, 16-20]. Nevertheless, considering only monovacancy trapping is clearly an oversimplification of the actual situation, as vacancy clusters were clearly identified in many irradiation experiments[21-24]. Recently, we have developed predictive models to enable accurate predictions of vacancy-vacancy clustering behavior and H-vacancy cluster interaction for arbitrary sized vacancy clusters in bcc metals [25, 26]. These predictive models serve as a foundation for feeding data into an object kinetic Monte Carlo (OKMC) framework, enabling multi-scale modelling that allows for a quantitative assessment and analysis of H retention and desorption behavior in PFM [26, 27].

In this study, utilizing OKMC simulations, we delve into the behavior of D within Mo subjected to 1 MeV self-irradiation. Our findings unveil the substantial contribution of vacancy clusters to deuterium diffusion, trapping, and desorption, with the formation of vacancy clusters significantly influencing the TDS of D. Furthermore, our analysis indicates a saturation of D retention at elevated damage levels. Under conditions of constant temperature storage, our observations reveal a non-exponential desorption rate, showcasing a decrease over time proportional to 1/t. This study reveals the intricate relationship between deuterium and vacancy clusters in irradiated materials, emphasizing their crucial role in modeling deuterium retention and desorption, vital for fusion reactor material studies.

2. Computational method

2.1 General algorithm

The OKMC method [28] is a powerful computational approach for studying the long-term evolution of defects in materials. The fundamental principles underlying OKMC simulations of defects revolve around selectively considering thermal fluctuations that lead to transitions, such as defect migration and dissociation, thus capturing the evolution of defects. Different from the conventional KMC method, here we do not explicitly track the trajectory of each atom, but instead treat defect clusters as individual objects with specific positions, reaction volumes, and spherical shapes assumed.

Specifically, in our OKMC simulations, events occur randomly at each Monte Carlo step, with the probability of each event determined by its activation rate Γ. These events comprise defect migration, rotation of migration direction, and point defect emission or de-trapping from a defect cluster, all considered as internal events. The activation rates of these internal events are governed by the Arrhenius relation, given as:

$$\Gamma_i^{int} = \upsilon_i \exp\left(-E_{a,i}/k_B T\right),$$

where υ_i and $E_{a,i}$ denote the activation energy and attempt frequency for event *i* respectively, k_B is the Boltzmann constant and *T* is the absolute temperature of system. Additionally, we incorporate external events such as ion implantations and the creation of primary damages. The activation rate for an external event is expressed as:

$$\Gamma^{ext} = f \times S,$$

where f denotes the implantation flux, and S represents the area of the simulation box surface normal to the implantation direction. In the case of an external event being selected, the OKMC simulation involves the random extraction of an ion from a pre-tabulated implantation database (see Section 2.3 below). Subsequently, the chosen ion, along with the primary damage defects it generates, are inserted into the simulation box. Following execution of a selected event, the advancement of simulated time follows the residence time algorithm, given by $\Delta\tau = 1/\left(\Sigma_{i=1}^{N_{int}} \Gamma_i^{int} + \Gamma^{ext}\right)$,[29, 30], where N_{int} represents the number of internal events. In addition to the rate-driven events discussed earlier, our OKMC model also considers non-rate-driven events, such as defect clustering/trapping or surface desorption. Typically, these events are exothermic and manifest instantaneously when overlapping reaction volumes are detected, thereby incurring no or ignorable time increment to the system. During the course of OKMC simulations, events are iteratively selected and executed until a specific target time is attained.

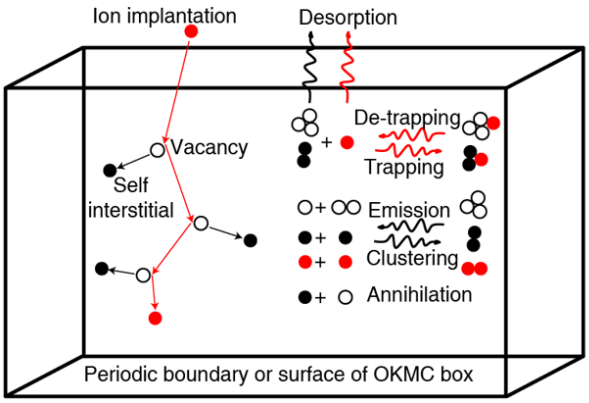

Fig. 1. (color online) Schematic of the simulation box and main events in the OKMC model [27].

2.2 Parameterization of OKMC model

In our OKMC model, we aim to minimize the use of adjustable parameters, with the process encompassing two key aspects, i.e., *i*) the establishment of an implantation database for Mo/D ions and *ii*) compilation of kinetics, energetics, and geometrical properties for various defects.

For the first aspect, the implantation of Mo/D isotopes, we employed an open-source program called "IM3D," which follows a similar approach to SRIM (Stopping and Range of Ions in Matter). This program was used to model the stopping behavior of 1 MeV Mo ions (as well as 200 eV D ions) in Mo, along with the primary damages they induced. A comprehensive description of this method can be found in the work by Li et al. [31]. Mo/D ions were implanted vertically into a pristine Mo bulk sample. Each ion was individually implanted without any memory or interaction with previously implanted ions, as these interactions are handled by the OKMC method. For atomic displacements in Mo, a threshold energy of 34 eV was applied [32]. After an ion was implanted into the Mo bulk, the positions of the stopped ion (unless it was backscattered) and the primary damage defects were recorded in an implantation database. For each implantation energy, 1,000 ions were implanted, which was found to be sufficient to achieve statistical convergence.

For the second aspect, we referred to existing DFT studies in parameterizing defect properties. We began by tabulating migration-related properties, including migration attempt frequency, migration barrier, and migration distance, for vacancies (V_1), self-interstitial atoms (SIA_1), and D interstitials. It is worth noting that DFT data for V_n and SIA_n clusters (the subscript n denotes the number of vacancies/SIA in the cluster, similar notations are used for H clusters and H-V/SIA complexes in below) are relatively scarce. Hence, we adopted a strategy similar to that used by Becquart et al. [33], where a constant migration barrier was assigned to all V_n and SIA_n clusters, and their attempt frequency was varied based on cluster size. This approach was also extended to D interstitials. Furthermore, based on our previous investigation [34], it was determined that D does not form clusters due to the relatively low implantation flux used in our current work. Therefore, we did not consider H_n clusters in this particular study. For other defects, such as D-vacancy and D-SIA complexes, we assigned a very high migration barrier, rendering them effectively immobile.

Table 1. Migration attempt frequency ($\boldsymbol{\upsilon}$), migration barrier ($\boldsymbol{E_m}$), and migration distance ($\boldsymbol{d}$) for vacancie clusters ($\boldsymbol{V_n}$), self-interstitial atom (SIA) clusters ($\boldsymbol{SIA_n}$), and D interstitial ($\boldsymbol{D_1}$), where the integer $\boldsymbol{n}$ denotes the vacancy or SIA cluster size . Defects not listed here are considered immobile. The values of the constants are $\upsilon_0 = 6$ THz, $\upsilon_H = 27.7$ THz, $q = 1000$, and $a_0 = 3.147$ Å.

	υ (THz)	E_m (eV)	d	Comments	Ref.
V_n	$\upsilon_0 q^{1-n}$	1.2	$\frac{\sqrt{3}a_0}{2n}$	3D motion	[33, 35]
SIA_n	$\upsilon_0 n^{-0.5}$	0.064	$\frac{\sqrt{3}a_0}{2n}$	1D motion, with 0.18 eV rotation barrier for n=1	[33, 36]
D_1	υ_H	0.16	$\frac{\sqrt{2}a_0}{4}$	3D motion	[37]

Next, we determine the binding energy between two defects (or defect clusters) A and B, defined as:

$$E_b^{A,B} = E^A + E^B - (E^{A+B} + E^{bulk}), \tag{1}$$

where E^A, E^B, and E^{A+B} respectively represent the energy of a system containing defect A, B, and A+B combo, and E^{bulk} is the energy of the reference defect-free system.

With this definition, we first determine the binding energy between a vacancy and a vacancy cluster, using the formula developed in our previous work [25]:

$$E_b^{V_1,V_{n-1}} = E_f^{V_1} - \left(E_f^{V_2} - E_f^{V_1}\right)\frac{\Delta S_{WS}^{V_n}}{\Delta S_{WS}^{V_2}}, \tag{2}$$

where $E_f^{V_1} = 2.68$ eV and $E_f^{V_2} = 5.41$ eV are formation energies of V_1 and V_2 respectively, $\Delta S_{WS}^{V_n}$ is the surface area difference between Wigner-Seitz cells of V_n and V_{n-1} clusters.

The binding energy between a SIA and SIA clusters is calculated using the capillary law [33]:

$$E_b^{SIA_1,SIA_{n-1}} = E_f^{SIA_1} + \left(E_b^{SIA_1,SIA_1} - E_f^{SIA_1}\right)\frac{n^{\frac{2}{3}} - (n-1)^{\frac{2}{3}}}{2^{\frac{2}{3}} - 1}, \tag{3}$$

where $E_f^{SIA_1} = 7.45$ eV according to ref. [36]. No DFT data on $E_b^{SIA_1,SIA_1}$ is available to our best knowledge, the corresponding data for W, $E_b^{SIA_1,SIA_1} = 2.12$ eV [33], was used in this study considering the similarity between W and Mo. We employ these approximations due to the high binding energies exhibited by SIA clusters, especially when compared with their exceedingly low diffusion barriers (refer to Table 1). Consequently, the prospect of SIA cluster dissociation preceding their annihilation becomes virtually implausible. Therefore, the precise determination of $E_b^{SIA_1,SIA_{n-1}}$ assumes negligible

significance, so long as it remains a substantially elevated value.

The binding energy between a D and a V_nD_{m-1} complex is determined by:

$$E_b^{V_nD_m} = E_D^{TIS} - E_D^{V_nD_m}, \tag{4}$$

where $E_H^{TIS} = 0.76\,\text{eV}$ is D energy level at tetrahedral interstitial site in Mo (for binding energy calculations, zero-point energy (ZPE) correction is included for D atoms by summing up their ground state vibration energies to ensure accurate description of the energetics), and $E_D^{V_nD_m}$ is D energy level in the V_nD_m cluster, which is given by solving [26]:

$$E_D^{V_nD_m} = \frac{3}{2}A_c\left(\frac{m_c}{v}\right)^2 = E_{n_s}^{ij} + 7.3A_s\left(\frac{m_s}{s}\right)^{2.5}, \tag{5}$$

and:

$$m = m_c + m_s. \tag{6}$$

Here, $A_c = 8.01\ \text{eV}\cdot\text{Å}^6$, $A_s = 3.32\ \text{eV}\cdot\text{Å}^5$, $s = 4\pi r^2$, $r = a_0\left(\frac{3n}{8\pi}\right)^{\frac{1}{3}}$, $v = \frac{4\pi}{3}(r - 0.97)^3$. $E_{n_s}^{ij}$ is the energy level of the n_s^{th} D adsorption on a ij type of Wigner-Seitz square of the V_n vacancy cluster (XXX explain a bit here, and add some schematic in suppinfo XXX see details in Ref. [26]). The values of $E_{n_s}^{ij}$ are -0.43, -0.53, -0.62, -0.78, and -0.55 eV for ij = 10, 11, 12, 21, and 22, respectively.

It is important to note that SIAs and SIA clusters exhibit rapid diffusion at 300 K and thus would quickly annihilate through interactions with vacancies or at the boundaries or free surfaces. Therefore, no SIAs are expected to be present at the initiation of D charging, which was also confirmed in our simulations. Consequently, we excluded the consideration of SIA-D interactions in this study. The binding energies, as predicted by Eqs. (2-6), are partially demonstrated in Fig. 2. Additionally, the de-trapping energy of a defect is determined by the summation of the binding energy and the migration energy barrier associated with the relevant defects. For instance, the energy required for a defect A to de-trap from a defect cluster AB is given by:

$$E_t^{AB-A} = E_b^{A,B} + E_m^A. \tag{7}$$

Here, E_m^A represents the migration barrier of defect A. Following de-trapping, defect A will migrate one step away from defect B and no longer interact with B over long distances, unless they diffuse again and their capture volumes overlap. It is important to mention that based on the DFT data provided, trap mutation is generally unfavorable, implying that V_nH_m clusters cannot grow through the emission of a SIA. Notably, all energies discussed above were calculated at 0 K with ZPE for D, and the phonon free energy were not considered in these calculations as it's generally negligible at room temperature [38]. The full parameter set of defect properties can be found in the supplementary information

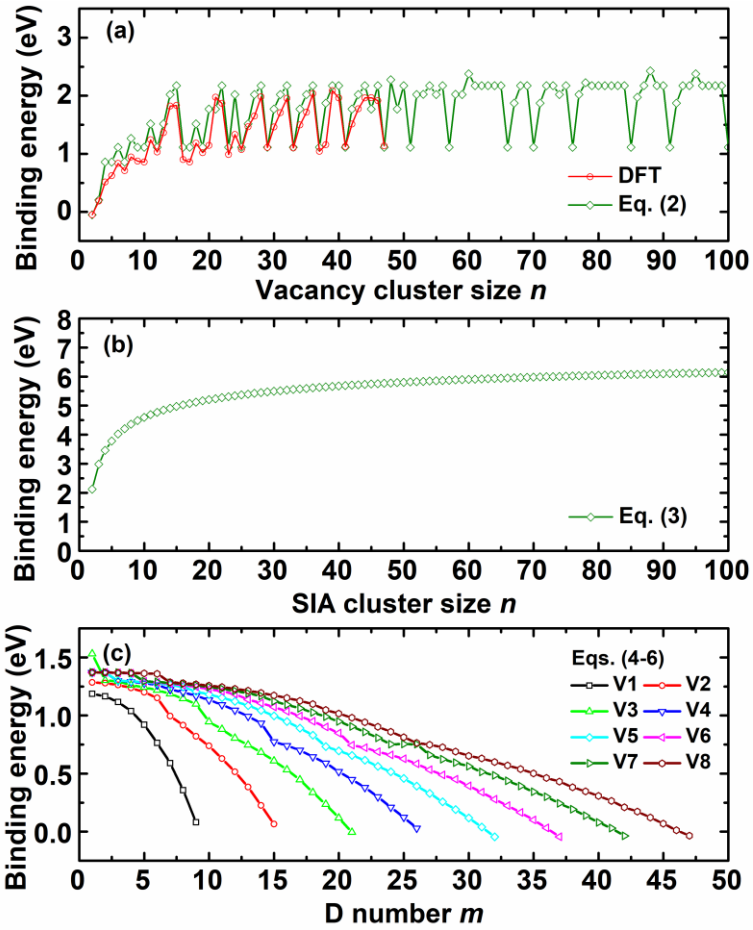

Fig. 2. (color online) Binding energies of (a) a single vacancy to vacancy clusters of different sizes, (b) a SIA with SIA clusters of different sizes, and (c) D with V_nD_m complexes as the complex size varies (with ZPE correction).

3. OKMC results

3.1 Calibration with experiments

Our OKMC model was calibrated by using experiment set-ups that used in Lavrentiev et al.'s recent work[7]. The main simulation parameters are summarized in Table 2 and briefly reviewed here. For starters, we created a pure Mo sample in our OKMC simulations, then irradiated it with 1 MeV Mo self-ions with a flux of $1.05 \times 10^{14}\ ion/m^2/s$ and fluences between $1.05 \times 10^{16-18}\ ion/m^2$, corresponding to damage levels of 0.01-1 dpa in the surface layer of 200 nm. After the self-ion irradiation, the sample was kept in vacuum for 1 hour, then implanted with 200 eV and $10^{18}\ ion/m^2/s$ D ions for a duration of 5 hours, corresponding to a fluence of $1.8 \times 10^{22}\ ion/m^2$. The sample was stored in vacuum again after the implantation for a time period of 1 day or 30 days. After that, we carried out the thermal desorption spectrum (TDS) simulation by heating up the sample with a constant heat rate of 10 K/m up to 1000 K. All simulations were performed at 300 K except the TDS simulation.

Table 2: Main experimental parameters used in calibrating our OKMC model. E_{ion} is the kinetic energy of

implanted ions, f and F is the implantation flux and fluence, T is the implantation temperature.

	E_{ion}	f (ion/m^2/s)	Time	T (K)
Self-ion irradiation	1 MeV	1.05×10^{14}	100-10,000 s	300
Storage	/	/	1 h	300
D charging	200 eV	1.0×10^{18}	5 h	300
Storage	/	/	1-30 d	300
Thermal desorption	/	/	/	300 +10 K/m

In our OKMC model, the supercell is subjected to periodic boundary conditions (PBC) in the first two dimensions, as depicted in Fig. 1. Mo/D ions are implanted into the supercell from the top surface of the third dimension and can undergo desorption from both the top and bottom surfaces of this dimension. For all our OKMC simulations, we utilized a supercell with dimensions of $30 \times 30 \times 2000\ nm^3$. Through thorough examination, we ensured that this supercell size is sufficiently thick to prevent the majority of irradiation defects and implanted ions from being released at the bottom surface. Moreover, any further increase in the supercell thickness has been found to yield only negligible changes in our simulation results.

3.2 MeV Mo self-ion irradiation

We started by conducting simulations of 1MeV Mo self-ion irradiation, demonstrating the distribution of defects at three dpa levels (Figs. 3a-3c). The green clouds represent residual cascade damage containing high-density self-interstitial atoms (SIA) and vacancy-type defects. The total number of SIA-type defects induced would be approximately equal to that of vacancy-type defects, except for the near-surface region due to possible sputtering. Post irradiation, the SIA-type defects, highly mobile at 300 K (Table 1) in comparison to vacancy-type defects, would quickly diffuse and annihilate at the sample surface or its close vicinity, leading to net vacancy accumulation in the bulk region. Meanwhile, despite vacancy-type defects being rather immobile, we noticed the formation of vacancy clusters. We also noticed the formation of vacancy clusters (Vn≥6) despite the immobility of vacancy-type defects. These clusters were found to form either in cascade core regions with high density of vacancies, or from the overlapping of irradiation cascades with vacancies from prior events. As the dpa level increases, the density of vacancies and vacancy clusters also increases. In the 1 dpa case, an additional snapshot was taken one hour after the irradiation, revealing the rapid annihilation of all SIA-type defects, leaving only vacancy-type defects in the system.

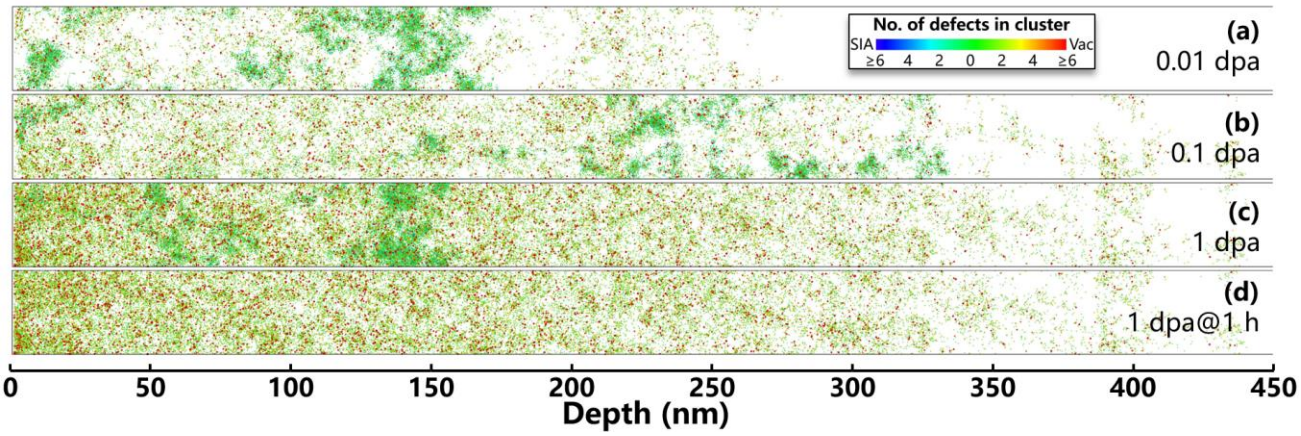

Fig. 3. (color online) Snapshots of OKMC simulations of 1 MeV Mo self-ion irradiation at (a) 0.01 dpa, (b) 0.1 dpa, (c) 1 dpa, and (d) 1 hour after 1 dpa irradiation, at temperature $T = 300$ K.

The distribution and evolution of vacancies during irradiation were then analyzed to gain quantitative insights into the 1 MeV Mo self-ion irradiation process. Fig. 4a shows the population of vacancy clusters at three dpa levels. Starting from the 0.01 dpa case, we can see that the evolution curve exhibits an exponential decay with respect to cluster size (vertical axis in logarithm scale). Intriguingly, such exponential decay in the vacancy cluster size remains unaltered as the dpa level escalates, except for a uniform upward shift in the curve. Another observation from the results is that over 70% of the vacancies are in the form of vacancy clusters, rather than monovacancies, in all three cases. This finding raises a critical question about validity of the monovacancy approximation which is frequently employed in modeling irradiation and subsequent processes involving D retention and desorption[7, 16-20].

We further investigated the depth distribution of vacancies (in both monovacancies and vacancy clusters) by evaluating their concentration profiles at the three damage levels, depicted in Fig. 4b. Significant enrichment of vacancies in the near-surface region was observed, along with quick decay in vacancy concentration as the depth increases. The quick decay results in vacancy depletion in the bulk region, and as seen in Fig. 4b, such depletion occurs for depth beyond 400 nm, for all three dpa levels examined. These observations of vacancy distribution stem from the interplay between two competing processes of SIA absorption at the sample surface and vacancy-SIA annihilation. Particularly for the near-surface vacancy enrichment, it results from the higher likelihood of SIA absorption at the near-surface region and thus reduced occurrence of vacancy-SIA annihilation events, consequently rendering the region vacancy abundant. We also noted that t the accrual of defects does not adhere to a linear relationship with respect to the dap level. This phenomenon is graphically depicted in Fig. 4c, wherein the average concentration of vacancies within the depth range of 0-400 nm is presented as a function of the dpa level. Intriguingly, our observations reveal a rapid increase in the accumulated vacancy concentration at low dpa levels, followed by a notable deceleration in accumulation as the dpa level increases, hinting at a potential saturation phenomenon. This behavior closely aligns with numerous prior experimental observations indicating that D retention reaches a

saturation point at a damage level around several tens of dpa, as comprehensively summarized by Schwarz-Selinger in[3]. Upon analyzing our OKMC data, we have identified that this saturation emerges due to an escalated rate of vacancy-SIA annihilation. This augmented rate can be attributed to the increased concentration of vacancies, leading to a gradual flattening of the vacancy accumulation curve.

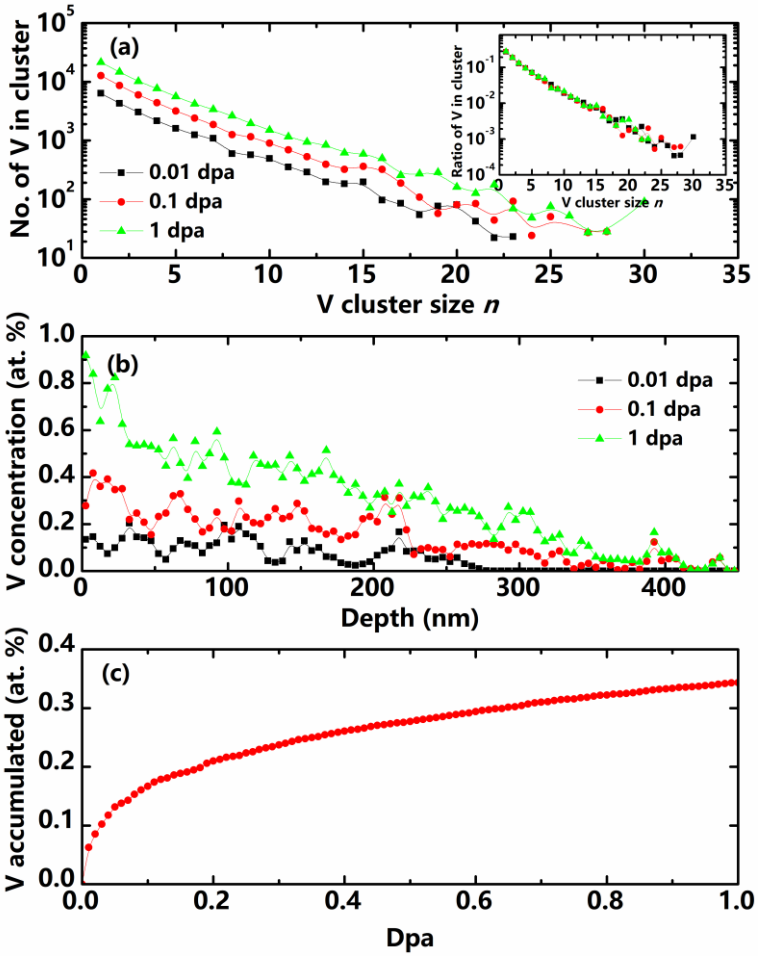

Fig. 4. (color online) Evolution of vacancies during 1 MeV Mo self-ion irradiation. (a) Vacancy cluster size distribution at different dpa levels, the embedded figure show corresponding ratio distribution. (b) Vacancy depth distribution at different dpa levels. (c) Average vacancy concentration within the 0-400 nm depth as a function of dpa level.

3.3 Deuterium charging in irradiated Mo sample

Upon completion of the afore-mentioned irradiation procedure, the irradiated samples were then subjected to charging with 200 eV D plasma, simulating the service environment typically encountered by plasma-facing components. As a representative example, the 1 dpa Mo sample was utilized, and the corresponding dynamic evolution of D penetration during the charging process is depicted in Fig. 5. Notably, a well-defined boundary delineating the region where irradiation defects are decorated with

D atoms from the D-free region can be observed. As the charge time increases, this boundary progressively advances into the bulk, leading to a consistent incremental growth in penetration depth across successive snapshots, ultimately reaching approximately 180 nm after 5 hours of charging. Another notable observation from Fig. 5 is that the growth in penetration depth in successive snapshots whose corresponding charging times scale with $\sqrt{t}$ appears approximately uniform. This indicates a linear dependence of the penetration depth on $\sqrt{t}$, thereby revealing the characteristic features of a typical diffusion-controlled process and the underlying mechanisms governing D ion diffusion within the irradiated sample.

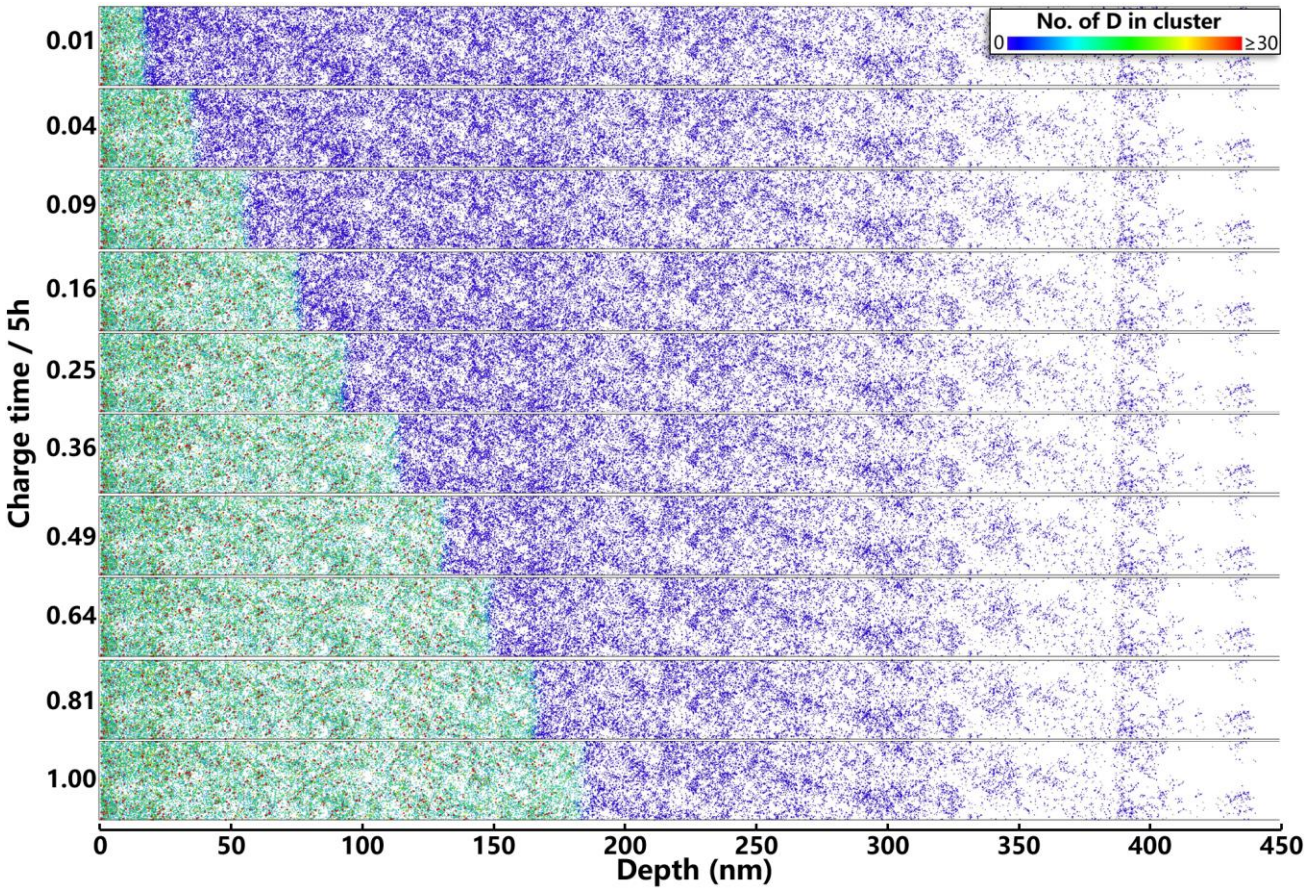

Fig. 5. (color online) Snapshots of OKMC simulation results of D charging in the 1 dpa Mo sample, at 300 K and different charging time *t*. Note that the charging times of the snapshots scale with $\sqrt{t}$.

In addition the results shown in Fig. 5, we further investigated the diffusion dynamics of D in irradiated samples by analyzing the concentration profiles of D at varying charge times, shown in Fig. 6a. Notably, we can observe a upper boundary curve, effectively capping the maximum D concentration at different depths. Such upper boundary curve reflects the saturation phenomenon arising from D occupying vacancy-type defects. The saturation value of D as a function of the depth exhibits a rapid decay within the first 50 nm, subsequently stabilizing between 50-150 nm, a trend in accordance with the vacancy concentration profile illustrated in Fig. 4b. Consistent with the earlier

observation in Fig. 5, we also note the steady advancement of the D concentration profile into the bulk, with an approximate uniform pace of advancement in the depth with respect to $\sqrt{t}$.

For a more quantitative assessment of D charging behaviors, we introduced a penetration depth parameter x, defined as the depth at which D concentration reaches 1% (approximately half of the saturation concentration within the 50-150 nm plateau, c.f., Fig. 6a), and investigated its evolution as a function of the charging time. Interestingly, Fig. 6b reveals an exceptional linear relationship between squared penetration depth and charge time, culminating in an insightful revelation concerning the diffusion kinetics of D within the irradiated material. Here, by assuming $\xi_{eff} = x^2/t$, we deduce an effective diffusivity, $\xi_{eff} = 1.91\ nm^2/s$, for D in the damage zone. It is noteworthy that this value significantly contrasts with the diffusivity of D in Mo, $\xi_0 = 2.35 \times 10^8\ nm^2/s$, obtained with OKMC simulation employing a pristine Mo.

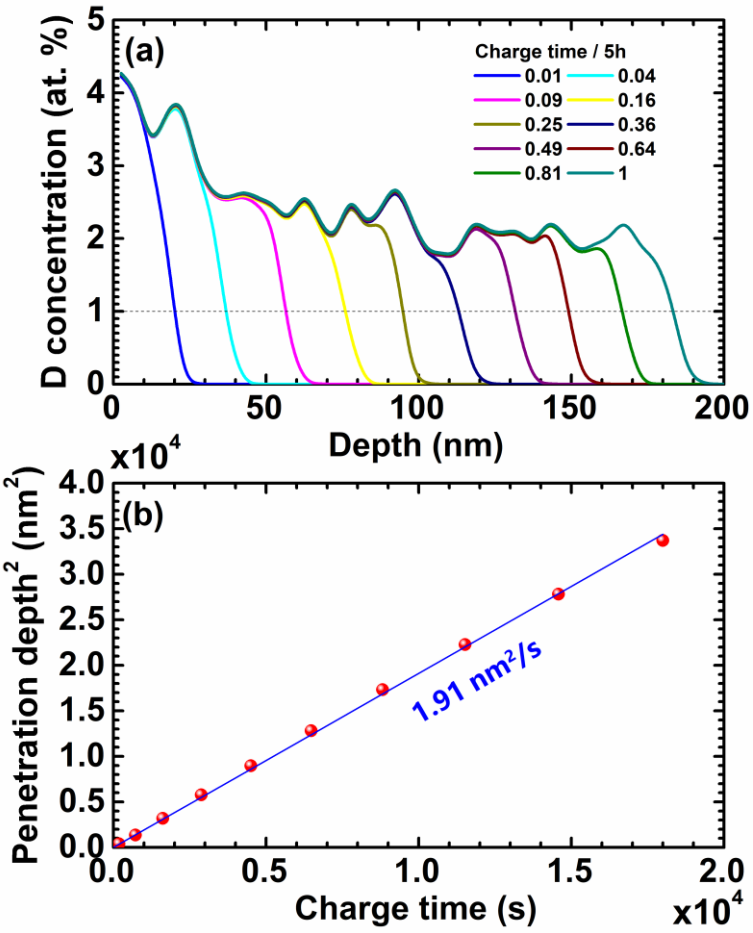

Fig. 6. (color online) Evolution of deuterium concentration in the 1 dpa Mo sample during plasma charging. (a) Concentration profiles at different charge times, (b) relationship between squared penetration depth (depth with D concentration of 1%) and charge time, with the blue line representing the linear fitting of OKMC results.

The drastic reduction in diffusivities of D underscore the profound influence of vacancy trapping

on its diffusion dynamics, which can be effectively estimated using the Mac-Nabb and Forester formula [39]:

$$\xi_{eff} = \frac{\xi_0}{1 + \sum_i c_i \exp\left(E_i^b / k_b T\right)}, \tag{8}$$

where c_i is the concentration of trapping site i and E_i^b is its binding energy with D. Considering the presence of multiple types of vacancy clusters, each with the capacity to trap numerous D atoms possessing different binding energies (E_i^b), accurately evaluating c_i and E_i^b proves to be a challenging task. To simplify the analysis, we adopt a single trap concentration of $\sum_i c_i = 0.5\%$ (representing the average vacancy concentration within the 0-200 nm depth) in Eq. 8. Subsequently, employing the values of D_0 and ξ_{eff} obtained previously, we solve the equation, yielding an average binding energy of $\overline{E_i^b} = 0.62\ eV$. This value signifies the effective binding energy of a mobile D interstitial with various V_nD_m clusters. Fig. 7 presents a statistical distribution of different V_nD_m clusters at the conclusion of D charging. It becomes evident that the dominant cluster types include V_1D_6, V_2D_{10}, V_3D_{14}, and V_4D_{17}, with their associated binding energies to an additional D being 0.59, 0.63, 0.61, and 0.64 eV, respectively (as illustrated in Fig. 2c), exhibiting an excellent agreement with the $\overline{E_i^b} = 0.62\ eV$ derived earlier. This remarkable concurrence further validates our insights into the effective binding energies, providing valuable data for understanding the intricate interplay between D and vacancy clusters in the irradiated material. (add some discussion on max/effective binding energy)

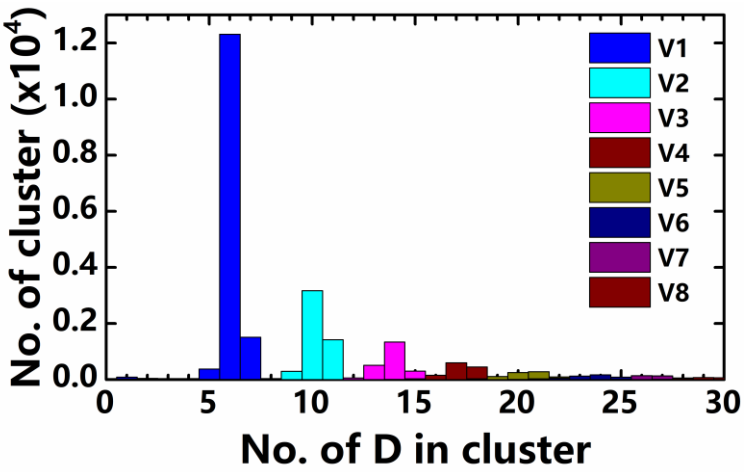

Fig. 7. (color online) Number of D atoms in the vacancy cluster V_n at the end of D charging in the 1 dpa irradiated Mo sample.

4. Deuterium desorption in bcc irradiated Mo

4.1 Modelling TDS from OKMC simulations

Following the completion of D plasma charging in irradiated Mo samples, we proceeded with investigations of the desorption behavior of D from these materials. Fig. 8a illustrates the thermal desorption spectrum (TDS) for Mo samples irradiated at varying levels of dpa. Notably, we observe a higher desorption rate in the high dpa sample compared to the low dpa sample, which can be attributed to the elevated concentration of irradiation-induced vacancies in the former, thereby providing more trapping sites for D atoms. All TDS curves display significant breadth, spanning temperatures from 300 K to 700 K, with half-peak widths of 200-250 K, indicative of D atoms being trapped at defects with diverse trapping energies. As the dpa level increases from 0.01 to 1 dpa, the peak temperature of TDS also shifts from 520 K to 580 K. This observation can be attributed to larger vacancy clusters exhibiting stronger binding energies with D, as previously demonstrated in Fig. 2c, implying that these clusters may play a more significant role in the TDS behavior of high dpa samples. Furthermore, we explored the influence of post-charge storage time on the TDS of the 1 dpa sample. Remarkably, extending the storage time from 1 day to 1 month leads to a substantial reduction in the D desorption rate at temperatures below 440 K, while no significant alteration occurs in the high-temperature region. This outcome can be attributed to the high-temperature desorption process, which involves D de-trapping from defects with relatively strong D trapping energy, remaining unaffected by an extended storage period. Fig. 8b depicts the overall amount of D released from the Mo samples, revealing a saturating trend concerning the dpa level. This behavior is evidently related to the saturation of vacancies, as discussed in Fig. 4c.

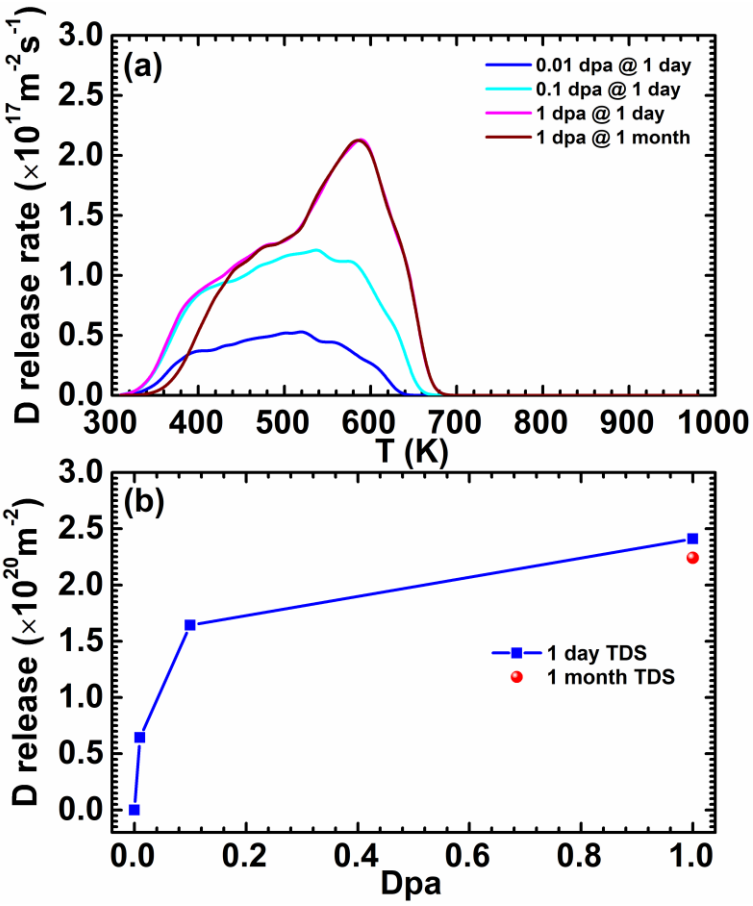

Fig. 8. (color online) Thermal desorption of deuterium from Mo samples irradiated to different dpa levels and with varying post-charge storage times. (a) Thermal desorption spectrum (TDS). (b) Overall deuterium release after charged at 300 K.

To gain a more profound understanding of the intricate processes governing D trapping and desorption, we conducted a comprehensive analysis of the thermal desorption spectrum (TDS) curves, focusing on the contributions of various vacancy clusters, as showcased in Figure 9. Our investigation reveals that these TDS curves comprise both monovacancies and vacancy clusters, with V_1 predominantly contributing to D desorption at temperatures below 500 K, while smaller clusters (V_{2-3}) dominate the desorption between 500-550 K, after which large vacancy clusters ($V_{\geq 4}$) take over at higher temperatures.

Strikingly, we observed unexpected negative desorption rate occurring between 460-540 K for large vacancy clusters. This intriguing phenomenon indicates an increase in the total number of D trapped within these clusters. This counterintuitive negative desorption arises from the activation of vacancy migration, facilitating the formation and growth of vacancy clusters, thereby transforming small $V_n D_m$ clusters into larger ones. Consequently, this leads to an enhanced desorption rate for small clusters and results in reduced desorption rates, even reaching negative values. In samples irradiated to high dpa levels, the phenomenon of negative desorption becomes more pronounced, primarily due to the presence of a relatively elevated vacancy concentration within these materials. This increased vacancy concentration creates favorable conditions for the formation and growth of vacancy clusters, which, in turn, contribute to the manifestation of negative desorption effects. This phenomenon is accompanied by a notable peak at approximately 600 K within the TDS curve of the 1 dpa samples, which signifies the heightened TDS contribution originating from large vacancy clusters.

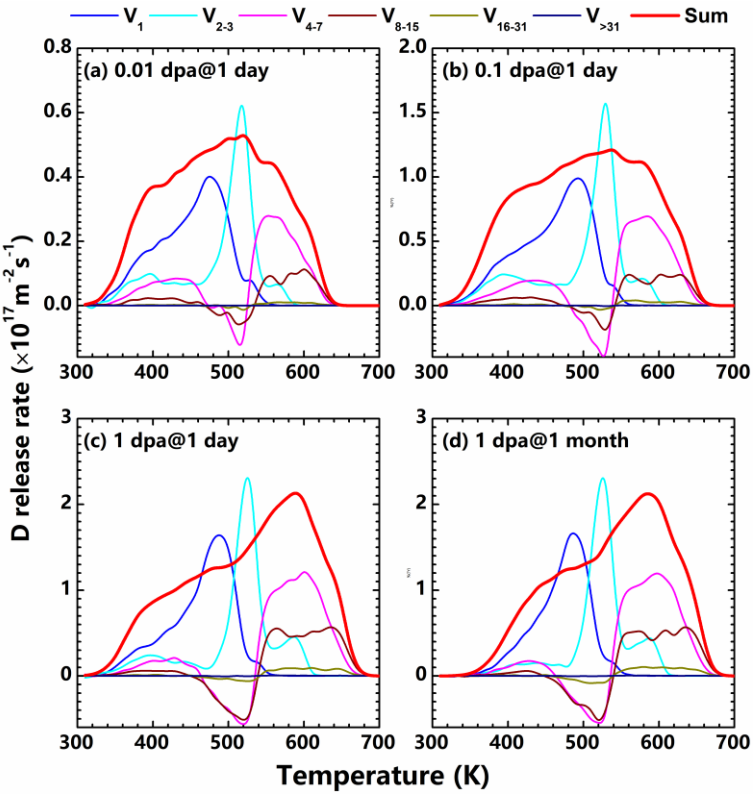

Fig. 9. (color online) TDS contributed by different vacancy clusters for (a) 0.01, (b) 0.1 and (c) 1.0 after one day and (d) 1.0 dpa after 30 days of irradiation . Note these figures are plotted with different scales.

The above reveals noteworthy findings regarding the migration and desorption of monovacancies and their impact on the formation of vacancy clusters in Mo samples. Notably, the migration energy of monovacancies is measured at 1.2 eV, which is lower than the maximum de-trapping energy of D from monovacancies, recorded at 1.35 eV. Consequently, vacancy migration is activated before monovacancies can entirely desorb all D atoms, thus leading to the formation of vacancy clusters. To elucidate this phenomenon, an additional simulation was conducted by manually removing vacancy clusters above a certain size from the 1 dpa sample, followed by D charging and TDS measurements. The results, presented in Fig. 10a, demonstrate a progressive reduction in the TDS peak around 600 K as vacancy clusters are gradually removed, underscoring the predominant contribution of large vacancy clusters to this peak. Interestingly, it was observed that even when all vacancy clusters were removed, and only monovacancies remained, the peak did not diminish to zero. To understand this behavior, a TDS contribution analysis was conducted for the sample with $V_{>1}$ clusters removed, as illustrated in Fig. 10b. Surprisingly, notable contributions from vacancy clusters were still evident in the TDS, despite their non-existence before the TDS measurement. This occurrence arises from the migration and clustering of monovacancies, as evidenced by the presence of negative desorption rates between 480-560 K. These compelling results highlight that the contribution of vacancy clusters to the TDS is inevitable, even when they are absent initially. Therefore, it is imperative to incorporate vacancy clusters in the understanding and modeling of D retention and desorption in Mo, as they play

a crucial role in shaping the material's response to plasma exposure.

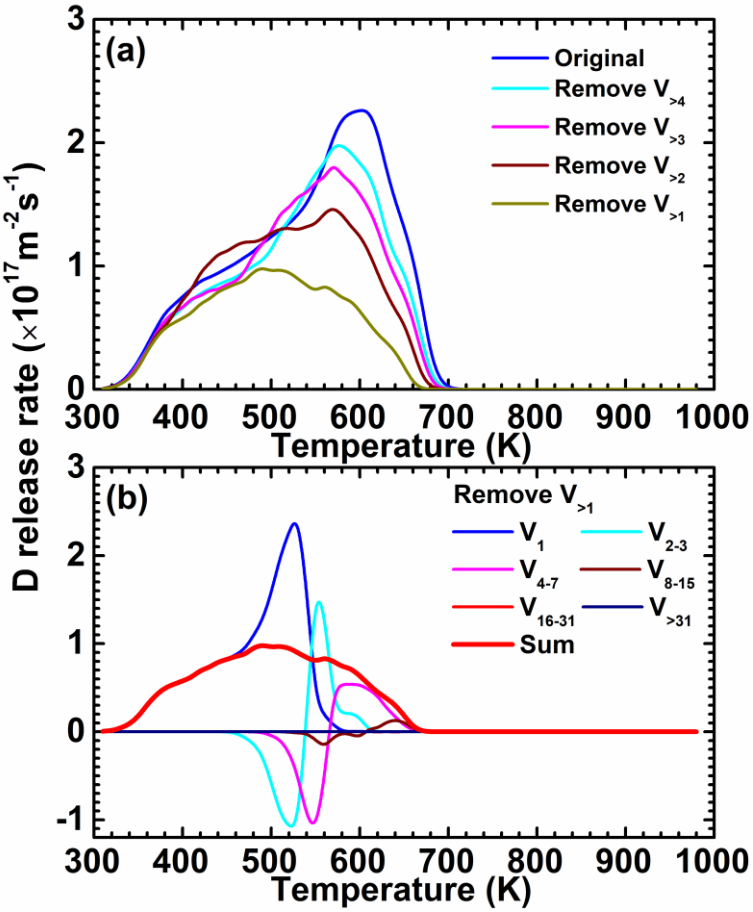

Fig. 10. (color online) Thermal desorption of deuterium from Mo samples with 1 dpa damage and 1-day post-charge storage time. (a) Thermal Desorption Spectroscopy (TDS) after manually removing vacancy clusters above certain sizes. (b) TDS contribution analysis for Mo sample with $V_{>1}$ clusters removed.

Apart from the thermal desorption spectrum which is measured by heating the sample to elevated temperatures, it's also important to understand the desorption behavior in storage conditions that usually involves not temperature changing. For this purpose, we perform OKMC simulations to determine the D retention and desorption during the storage period with a constant temperature. Fig. 11a shows the overall D retention evolution as a function of time. It's evident that samples stored at high temperatures release D much faster (note the logarithm time scale), with all D released in ~100 seconds at 700 K. While at 300 K, it takes ~10^{17} seconds (3.17 billion years) to completely desorb all D trapped. We also noted that as the D continue to desorb, further D desorption becomes more difficult and takes much longer timer. For instance, at 300 K, the desorption time required to reach 90%, 50%, and 10% retention is about 9 hours, 8000 years, and 100 million years, respectively. To understand this phenomenon, we calculated the desorption rate as a function of time with results demonstrated in Fig. 11b. Surprisingly, instead of showing an Arrhenius type exponential decrease as one would normally expect, the desorption rate follows a 1/t decrease against time throughout different temperatures.

In addition to investigating the thermal desorption spectrum, which entails heating the sample to elevated temperatures, it is also crucial to comprehend the desorption behavior under storage conditions where temperature remains constant. To address this, we employed OKMC simulations to examine D retention and desorption during the storage period. Fig. 11a presents the overall evolution of D retention as a function of time. Notably, samples stored at higher temperatures exhibit a significantly faster release of D, as evident from the logarithmic time scale, with complete desorption occurring in approximately 100 seconds at 700 K. In contrast, at 300 K, the process extends to an astonishing ~10^{17} seconds (equivalent to 3.17 billion years) for full desorption of trapped D. Furthermore, we observed that as D continues to desorb, further desorption becomes progressively more challenging and time-consuming. For instance, at 300 K, the time required to achieve 90%, 50%, and 10% retention reduces retention levels is approximately 9 hours, 8000 years, and 100 million years, respectively. To unravel this intriguing phenomenon, we conducted calculations of the desorption rate as a function of time, and the results, depicted in Fig. 11b, surprisingly deviate from the anticipated Arrhenius-type exponential decrease. Instead, the desorption rate exhibits a 1/t decrease against time across various temperatures. This unexpected behavior adds complexity to our understanding of D desorption kinetics, underscoring the need for further investigations to unravel the underlying mechanisms governing the desorption process.

The observed 1/t decrease pattern can be effectively elucidated through a multi-level trapping energy model, accounting for D atoms in both vacancies and vacancy clusters. Assuming that D desorption is primarily governed by de-trapping processes, we can formulate the time-dependent function of D retention as follows:

$$\frac{\partial N^i(t)}{\partial t} = N^i(t)C, \tag{9}$$

where $N^i(t)$ is the number of D atoms that remain trapped in trapping site i at time t, and C^i is a constant that given by:

$$C^i = v_0 \exp\left(-\frac{E_t^i}{k_B T}\right), \tag{10}$$

where E_t^i is the trapping energy, the pre-exponential factor v_0 is the attempt frequency of de-trapping (assumed to be a constant for all traps for simplicity). Solving the Eqs. (9-10) individually for each trapping site i, we have the overall retention function:

$$\frac{\partial N(t)}{\partial t} = \sum\nolimits_i N_{t=0}^i C^i \exp\left(-C^i t\right). \tag{11}$$

In Fig. 11c, the results calculated using Eq. (11) are presented, where we considered 9 trapping sites with trapping energies ranging from 1.0 to 1.4 eV, mimicking the multi-level trapping occurring in vacancies and vacancy clusters. For each type of trap, equal initial D atom population $N_{t=0}^i$ was considered. Remarkably, while the desorption rate of individual trapping energies exhibits an Arrhenius-type exponential decrease, the overall desorption rate (represented by the red line in Fig. 11c) manifests a 1/t decrease against time over a wide time range. This notable agreement with the

OKMC simulation results presented in Fig. 11b underscores the excellent predictive capability of the multi-level trapping energy model in explaining the observed 1/t decrease pattern in D retention.

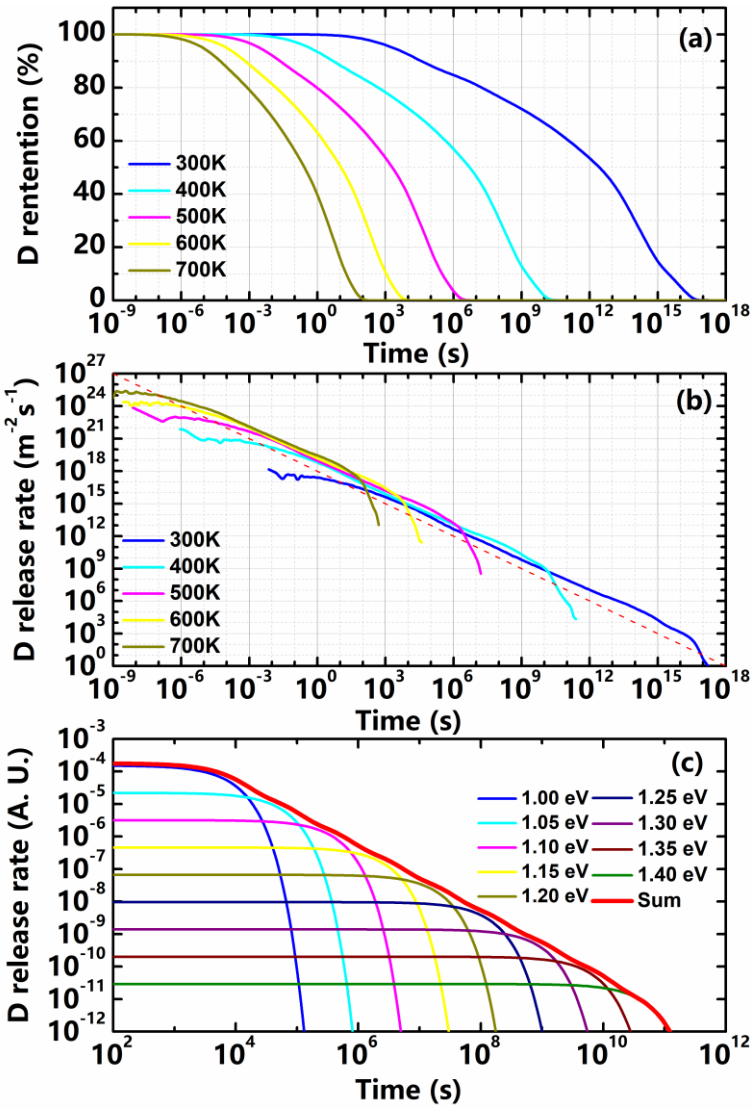

Fig. 11. (color online) Deuterium desorption behavior at constant temperatures in the 1 dpa Mo sample. (a) Deuterium retention from OKMC simulation. (b) Deuterium desorption rate from OKMC simulation, dotted line highlights a 1/t decay. (c) Deuterium desorption rate from Eq. 11 with various de-trapping energies.

4.2 Discussion

In the aforementioned simulations, we calibrated our OKMC model by referencing the experimental configurations outlined in Lavrentiev et al.'s recent study [7]. Their findings highlighted a prominent TDS peak occurring around 550 K, a trend that correlates closely with the observed peak temperatures falling within the range of 520-580 K, as depicted in Fig. 8a. Moreover, the experiments conducted by Lavrentiev et al. showcased an augmentation and eventual saturation of D content

between damage levels of 0.1 and 1 dpa. This also closely aligns with the saturation behavior depicted in Fig. 8b within our study.

While these notable agreements underscore the validity and accuracy of our simulation results, discrepancies persist between our simulations and experimental observations. For instance, Lavrentiev et al. speculated that the TDS peak to the desorption of D from monovacancies, whereas our study demonstrates that D atoms within vacancy clusters are the primary contributors to the TDS peak. Additionally, Lavrentiev et al. observed a small amount of D retention even at 0 dpa of irradiation damage, indicating D trapping at pre-existing defects like dislocations, impurities, or grain boundaries. This aspect warrants further attention in future OKMC models.

Furthermore, in Lavrentiev et al.'s experiments, a notable decrease in experimental D retention was observed after 1 month of storage at 300 K. This decrease was evident even in high-temperature regions of TDS (up to 620 K), which contrasts with our OKMC results where only the region below 440 K was affected in the TDS curve (see Fig. 8a). Notably, the TDS at 620 K primarily involved D with relatively strong trapping energies (approximately 1.4-1.5 eV), whereas Fig. 11c illustrates that it takes roughly $10^{10\text{-}11}$ s (~$10^{5\text{-}6}$ years) for these D atoms to escape at 300 K. Hence, understanding the significant reduction in high-temperature TDS poses a challenge. One plausible explanation for this disparity could be the existence of notable pre-existing H in Lavrentiev et al.'s experiments. These H atoms could potentially exchange with trapped D in strong trapping sites, without altering the total number of trapped isotopes. Consequently, this exchange may not be sensitive to the trapping energy of H or D and could readily occur at room temperature, significantly influencing the TDS of D in high-temperature regions. This highlights the need for further systematic investigations into isotope exchange effects in future studies.

5. Conclusion

In this computational study utilizing OKMC simulations, we explored the behavior of D in irradiated Mo samples. Our investigation highlighted the significant role of vacancy clusters in influencing D diffusion and trapping phenomena. The distinct distribution of vacancies and vacancy clusters in irradiated Mo was found to contribute significantly to D retention behavior. Additionally, the TDS analysis demonstrated a saturation effect in D retention at higher damage levels, with the presence of vacancy clusters leading to intriguing negative desorption rates at specific temperatures. Moreover, the study of D desorption under constant temperature storage conditions revealed a non-exponential desorption rate, displaying a 1/t decrease over time. These findings underscore the complex interplay between D and vacancies/vacancy clusters in irradiated materials. The consideration of vacancy clusters in the modeling of D retention and desorption processes is crucial for obtaining more accurate and comprehensive predictions. Our research provides valuable insights into the understanding of D behavior in irradiated Mo, paving the way for improved materials design and performance in future nuclear applications.

Acknowledgement

The work at UKAEA has been carried out within the framework of the EUROfusion Consortium, funded by the European Union via the Euratom Research and Training Programme (Grant Agreement No 101052200 — EUROfusion) and was partially supported by the Broader Approach Phase II agreement under the PA of IFERC2-T2PA02. Views and opinions expressed are however those of the author(s) only and do not necessarily reflect those of the European Union or the European Commission. Neither the European Union nor the European Commission can be held responsible for them.. We acknowledge Hefei Advanced Computing Center and Compute Canada for providing computing resources.

Data availability

The data generated and/or analyzed within the current study will be made available upon reasonable request to the authors.

Competing interests

The authors declare no competing interests.

[1.] Wright JAR. A review of late-stage tungsten fuzz growth. Tungsten. 2022.

[2.] Marian J, Becquart CS, Domain C, Dudarev SL, Gilbert MR, Kurtz RJ, et al. Recent advances in modeling and simulation of the exposure and response of tungsten to fusion energy conditions. Nuclear Fusion. 2017;57(9).

[3.] Schwarz-Selinger T. A critical review of experiments on deuterium retention in displacement-damaged tungsten as function of damaging dose. Materials Research Express. 2023.

[4.] Litaudon X, Abduallev S, Abhangi M, Abreu P, Afzal M, Aggarwal KM, et al. Overview of the JET results in support to ITER. Nuclear Fusion. 2017;57(10).

[5.] Andrew P, Brennan PD, Coad JP, Ehrenberg J, Gadeberg M, Gibson A, et al. Tritium retention and clean-up in JET. Fusion Engineering and Design. 1999;47:233-45.

[6.] Fukai Y. The Metal-Hydrogen System: Basic Bulk Properties. Second, Revised and Updated ed. Berlin, Heidelberg: Springer; 2005.

[7.] Lavrentiev MY, Hollingsworth A, Hess J, Davies S, Wohlers A, Thomas B, et al. Effects of self-irradiation on deuterium retention and reflectivity of molybdenum, fusion plasma-facing material: Combined experimental and modeling study. Journal of Applied Physics. 2022;132(12).

[8.] Alimov VK, Roth J, Lindig S. Surface modifications and deuterium depth profiles in molybdenum irradiated with low-energy D ions. Journal of Nuclear Materials. 2008;381(3):267-70.

[9.] Ogorodnikova OV. Ion-driven deuterium retention in high-Z metals. Journal of Nuclear Materials. 2009;390-391:651-4.

[10.] McCracken GM, Maple JHC. The trapping of hydrogen ions in molybdenum, titanium, tantalum and zirconium.

British Journal of Applied Physics. 1967;18:919.
[11.] Erents SK. Trapping and re-emission of deuterium from molybdenum following bombardment at 77 K. Vacuum. 1974;24:445-9.
[12.] You Y-W, Kong X-S, Fang QF, Liu CS, Chen JL, Luo GN, et al. A first-principles study on hydrogen behavior in helium-implanted tungsten and molybdenum. Journal of Nuclear Materials. 2014;450(1-3):64-8.
[13.] You Y-W, Kong X-S, Wu X-B, Xu Y-C, Fang QF, Chen JL, et al. Dissolving, trapping and detrapping mechanisms of hydrogen in bcc and fcc transition metals. AIP Advances. 2013;3(1):012118.
[14.] You Y-W, Kong X-S, Wu X-B, Fang QF, Chen J-L, Luo GN, et al. Effect of vacancy on the dissolution and diffusion properties of hydrogen and helium in molybdenum. Journal of Nuclear Materials. 2013;433(1-3):167-73.
[15.] Sun L, Jin S, Li X-C, Zhang Y, Lu G-H. Hydrogen behaviors in molybdenum and tungsten and a generic vacancy trapping mechanism for H bubble formation. Journal of Nuclear Materials. 2013;434(1-3):395-401.
[16.] Hodille EA, Ferro Y, Fernandez N, Becquart CS, Angot T, Layet JM, et al. Study of hydrogen isotopes behavior in tungsten by a multi trapping macroscopic rate equation model. Physica Scripta. 2016;T167:014011.
[17.] Ning RH, Li YG, Zhou WH, Zeng Z, Ju X. An Improved Cluster Dynamics Model for Hydrogen Retention In Tungsten. International Journal of Modern Physics C. 2012;23(06):1250042.
[18.] Ning RH, Li YG, Zhou WH, Zeng Z, Ju X. Modeling D retention in W under D ions and neutrons irradiation. Journal of Nuclear Materials. 2012;430(1-3):20-6.
[19.] Hu L, Li YG, Zhang CG, Zeng Z. Cluster dynamics simulation of deuterium retention behaviors in irradiated beryllium. RSC Adv. 2015;5(81):65750-6.
[20.] Zhao Z, Li Y, Zhang C, Pan G, Tang P, Zeng Z. Effect of grain size on the behavior of hydrogen/helium retention in tungsten: a cluster dynamics modeling. Nuclear Fusion. 2017;57(8).
[21.] Petersen K, Evans JH, Cotterill RMJ. Void formation during annealing of neutron-irradiated molybdenum. Philosophical Magazine. 1975;32(2):427-30.
[22.] Abe K, Masuyama T, Satou M, Hamilton M. Neutron irradiation damage and void lattice formation in a Mo alloy TZM. Materials Transactions, JIM. 1993;34:1137-42.
[23.] Sass SL, Eyre BL. Diffraction from void and bubble arrays in irradiated molybdenum. Philosophical Magazine. 2006;27(6):1447-53.
[24.] Observations of a Regular Void Array in High Purity Molybdenum irradiated with 2 MeV Nitrogen Ions. Nature. 1971.
[25.] Hou J, You Y-W, Kong X-S, Song J, Liu CS. Accurate prediction of vacancy cluster structures and energetics in bcc transition metals. Acta Materialia. 2021;211.
[26.] Hou J, Kong X-S, Wu X, Song J, Liu CS. Predictive model of hydrogen trapping and bubbling in nanovoids in bcc metals. Nature Materials. 2019;18:833.
[27.] Wang P, Cao Q, Hou J, Kong X-S, Chen L, Xie ZM. Implantation and desorption of H isotopes in W revisited by object kinetic Monte Carlo simulation. Journal of Nuclear Materials. 2022;561.
[28.] Domain C, Becquart CS, Malerba L. Simulation of radiation damage in Fe alloys: an object kinetic Monte Carlo approach. Journal of Nuclear Materials. 2004;335(1):121-45.
[29.] Young WM, Elcock EW. Monte Carlo studies of vacancy migration in binary ordered alloys: I. Proceedings of the Physical Society. 1966;89:735.
[30.] Bortz AB, Kalos MH, Lebowitz L. A new algorithm for Monte Carlo simulation of Ising spin systems. Journal of Computational Physics. 1975;17:10-8.
[31.] Li YG, Yang Y, Short MP, Ding ZJ, Zeng Z, Li J. IM3D: A parallel Monte Carlo code for efficient simulations of primary radiation displacements and damage in 3D geometry. Scientific reports. 2015;5:18130.
[32.] Jung P. Average atomic-displacement energies of cubic metals. Physical Review B. 1981;23(2):664-70.
[33.] Becquart CS, Domain C, Sarkar U, DeBacker A, Hou M. Microstructural evolution of irradiated tungsten: Ab initio

parameterisation of an OKMC model. Journal of Nuclear Materials. 2010;403(1-3):75-88.
[34.] Hou J, Kong X-S, Sun J, You Y-W, Wu X, Liu CS, et al. Hydrogen bubble nucleation by self-clustering: density functional theory and statistical model studies using tungsten as a model system. Nuclear Fusion. 2018;58(9):096021.
[35.] Smirnova D, Starikov S, Leines GD, Liang Y, Wang N, Popov MN, et al. Atomistic description of self-diffusion in molybdenum: A comparative theoretical study of non-Arrhenius behavior. Physical Review Materials. 2020;4(1).
[36.] Ma P-W, Dudarev SL. Symmetry-broken self-interstitial defects in chromium, molybdenum, and tungsten. Physical Review Materials. 2019;3(4).
[37.] Duan C, Liu Y-L, Zhou H-B, Zhang Y, Jin S, Lu G-H, et al. First-principles study on dissolution and diffusion properties of hydrogen in molybdenum. Journal of Nuclear Materials. 2010;404(2):109-15.
[38.] Kong X-S, Wang S, Wu X, You Y-W, Liu CS, Fang QF, et al. First-principles calculations of hydrogen solution and diffusion in tungsten: Temperature and defect-trapping effects. Acta Materialia. 2015;84:426-35.
[39.] McNabb A, Foster PK. A new analysis of diffusion of hydrogen in iron and ferritic steels. Transactions of the Metallurgical Society of AIME. 1963;227(3):618.